

Radio lobes and X-ray hot spots in the microquasar S26

Roberto Soria^{1*}, Manfred W. Pakull², Jess W. Broderick³, Stephane Corbel⁴,
Christian Motch²

¹*Mullard Space Science Laboratory, University College London, Holmbury St Mary, Surrey RH5 6NT, UK*

²*University of Strasbourg, CNRS UMR 7550, Observatoire Astronomique, 11 rue de l'Université, 67000 Strasbourg, France*

³*School of Physics & Astronomy, University of Southampton, Southampton, Hampshire SO17 1BJ, UK*

⁴*Université Paris 7 and Service d'Astrophysique, UMR AIM, CEA Saclay, F-91191, Gif sur Yvette, France*

Accepted ... Received ... in original form ...

ABSTRACT

We have studied the structure and energetics of the powerful microquasar/shock-ionized nebula S26 in NGC 7793, with particular focus on its radio and X-ray properties. Using the Australia Telescope Compact Array, we have resolved for the first time the radio lobe structure and mapped the spectral index of the radio cocoon. The steep spectral index of the radio lobes is consistent with optically-thin synchrotron emission; outside the lobes, the spectral index is flatter, suggesting an additional contribution from free-free emission, and perhaps ongoing ejections near the core. The radio core is not detected, while the X-ray core has a 0.3–8 keV luminosity $\approx 6 \times 10^{36}$ erg s⁻¹. The size of the radio cocoon matches that seen in the optical emission lines and diffuse soft X-ray emission. The total 5.5-GHz flux of cocoon and lobes is ≈ 2.1 mJy, which at the assumed distance of 3.9 Mpc corresponds to about 3 times the luminosity of Cas A. The total 9.0-GHz flux is ≈ 1.6 mJy. The X-ray hot spots (combined 0.3–8 keV luminosity $\approx 2 \times 10^{37}$ erg s⁻¹) are located ≈ 20 pc outwards of the radio hot spots (*i.e.*, downstream along the jet direction), consistent with a different physical origin of X-ray and radio emission (thermal-plasma and synchrotron, respectively). The total particle energy in the bubble is $\sim 10^{53}$ erg; from the observed radio flux, we estimate that only \sim a few 10^{50} erg are stored in the relativistic electrons; the rest is in protons, nuclei and non-relativistic electrons. The X-ray-emitting component of the gas in the hot spots contains $\sim 10^{51}$ erg, and $\sim 10^{52}$ erg over the whole cocoon. We suggest that S26 provides a clue to understand how the ambient medium is heated by the mechanical power of a black hole near its Eddington accretion rate.

Key words: galaxies: individual: NGC 7793 – X-rays: binaries – radio: galaxies – black hole physics.

1 INTRODUCTION

The basic physical model for radio lobes in FR II radio galaxies is based on a pair of relativistic, collimated jets emerging from the active black hole (BH). As the jet interacts with and is decelerated by the ambient (interstellar or intergalactic) medium, a reverse shock propagates inwards into the ejected plasma. After crossing the reverse shock, the jet material inflates a cocoon of hot gas, which is less dense but much overpressured with respect to the undisturbed medium. Thus, the cocoon expands supersonically, driving a forward shock (bow shock) into the ambient medium (Scheuer 1974; Blandford & Rees 1974; Begelman et al. 1984; Rawlings & Saunders 1991;

Kaiser & Alexander 1997). The cocoon and lobes are the main sources of optically-thin (steep spectrum) synchrotron radio emission, while we expect optically-thick (flat-spectrum) radio emission from the jet near the core. A radio- and sometimes X-ray-luminous hot spot is usually found at the reverse shock, at the end of the jet. This is where most of the bulk kinetic energy of the jet is transferred to thermal ions, and to a non-thermal population of ultra-relativistic electrons, which cool via synchrotron and synchrotron self-Compton emission. Non-thermal X-ray emission at the hot spot position may be due to synchrotron and synchrotron self-Compton emission. Optically-thin thermal plasma X-ray emission may come instead from the hot, shocked ambient gas between the reverse shock and the bow shock; in this case, the peak of the thermal X-ray emission will appear just in front of the radio hot spots.

* E-mail: roberto.soria@mssl.ucl.ac.uk

There is a scale invariance between the jet emission processes in microquasars (powered by stellar-mass BHs) and in AGN/quasars (powered by supermassive BHs). There is also at least one important difference: microquasars are mostly located in a relatively low-pressure medium as compared to the medium around AGN, when scaling of the jet thrust is taken into account (Heinz 2002). As a consequence, we expect to see fewer, dimmer cocoons and radio lobes in microquasars than in the most powerful AGN and quasars; however, the linear sizes of those microquasar cocoons and jets can be up to 1000 times larger than in radio galaxies, scaled to their respective BH masses. There is also evidence that some microquasars are located inside low-density cavities, compared with the undisturbed interstellar medium (Hao & Zhang 2009).

So far, our knowledge of the interaction of microquasar jets with the interstellar medium has largely relied on the Galactic microquasar SS 433 (Fabrika 2004) and its surrounding synchrotron-emitting nebula W50 (size $\sim 100 \times 50$ pc). A mildly relativistic ($v_J = 0.27c$), precessing jet acts as a sprinkler that inflates “ear-like” lobe structures, protruding from the more spherical W50 nebula. Most of the jet power ($\sim 10^{39}$ erg s^{-1}) is dissipated in the lobes (Begelman et al. 1980). Faint evidence of the interaction of relativistic jets with the interstellar medium has been found in a few other, less powerful Galactic microquasars: for example Cyg X-1 (Gallo et al. 2005), GRS 1915+105 (Kaiser et al. 2004), XTE J1550–564 (Corbel et al. 2002), H1743–322 (Corbel et al. 2005), and around the neutron star Sco X-1 (Fomalont, Geldzahler & Bradshaw 2001). On a larger scale, huge (size $\gtrsim 100$ pc) ionized nebulae have been found around several ultraluminous X-ray sources (ULXs) in nearby galaxies (Pakull & Mirioni 2002, 2003; Roberts et al. 2003; Pakull et al. 2006; Pakull & Grisé 2008; Grisé et al. 2008; Feng & Kaaret 2008). Such nebulae emit optical lines typical of shock-ionized gas, and in a few cases, synchrotron radio emission (Miller et al. 2005; Soria et al. 2006; Lang et al. 2007). The derived ages (\gtrsim a few 10^5 yr) and energy content ($\sim 10^{52}$ – 10^{53} erg) are too large for ordinary supernova remnants, and suggest jet/wind inflation with a mechanical power $\sim 10^{39}$ – 10^{40} erg s^{-1} , comparable with the X-ray luminosities (Pakull et al. 2006). However, no direct X-ray or radio evidence of a collimated jet has been found in ULX bubbles so far. On the other hand, X-ray luminous sources may be only a subset of non-nuclear BHs at very high mass accretion rates. Pakull & Grisé (2008) proposed that ionized bubbles might also be found associated with BHs that appear X-ray faint, either because their radiative emission is collimated away from our line of sight, or because they are transients and currently in a low/off accretion state, or because they channel most of their accretion power into a jet even at near-Eddington mass accretion rates.

2 THE MICROQUASAR S26 IN NGC 7793

A spectacular example of such systems was recently discovered (Pakull, Soria & Motch 2010, henceforth PSM10) in the outskirts of the Sculptor galaxy NGC 7793 (Figure 1), at a distance of 3.9 Mpc (Karachentsev et al. 2003). The radio/optical nebula S26 was originally classified as a su-

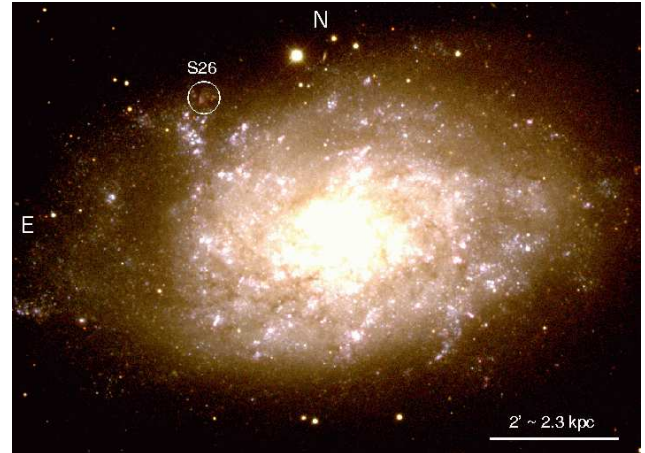


Figure 1. Location of S26 inside its host galaxy NGC 7793, from public-archive *BVR* images taken from the Cerro Tololo Inter-American Observatory (CTIO) 1.5-m telescope on 2001 October 18. S26 is inside the circle (radius of $15''$) in the north-eastern corner of the galaxy.

pernova remnant candidate (Blair & Long 1997); the high $[S\text{II}] \lambda 6716, 6732/H\alpha$ flux ratio indicates the presence of shock-ionized gas. The optical radial velocity of S26 agrees with that of NGC 7793, ruling out a chance superposition of a background AGN. A radio spectral index consistent with optically-thin synchrotron emission was reported by Pannuti et al. (2002), and the emitting region appeared clearly extended and elongated. However, the spatial resolution was too low to reveal details of its internal structure. A faint X-ray source was discovered to be associated with S26 in *ROSAT* observations (Read & Pietsch 1999), but it was unresolved. Using *Chandra* data, Pakull & Grisé (2008) discovered that the X-ray emission is resolved into three sources that are perfectly aligned and match the extent of the major axis of the radio and optical nebulae. Those sources have been interpreted as the core (at the X-ray binary position) and the X-ray hot spots (where the jet interacts with the ambient medium).

From optical spectroscopic observations, PSM10 determined the expansion velocity, density and temperature of the line-emitting gas in the bubble, and discovered that the mechanical power of the central BH is \sim a few $\times 10^{40}$ erg s^{-1} ; this suggests accretion rates similar to those required for the most luminous ULXs. PSM10 showed that the jet power is orders of magnitude higher than both the X-ray luminosity and the value one would derive from the radio luminosity; they argued that most of the jet power is transferred to non-relativistic protons and nuclei rather than non-thermal relativistic electrons.

In this paper, we present the initial results of our radio study, showing for the first time the resolved lobe structure and measuring the spectral index variations across the source. We discuss the origin of the radio emission and the implied jet power. We compare the radio, X-ray and optical maps of the nebula, determining the positions of the radio and X-ray hot spots and of the core, and we provide a more detailed spectral analysis and interpretation of the X-ray properties. We then summarize the energy budget of

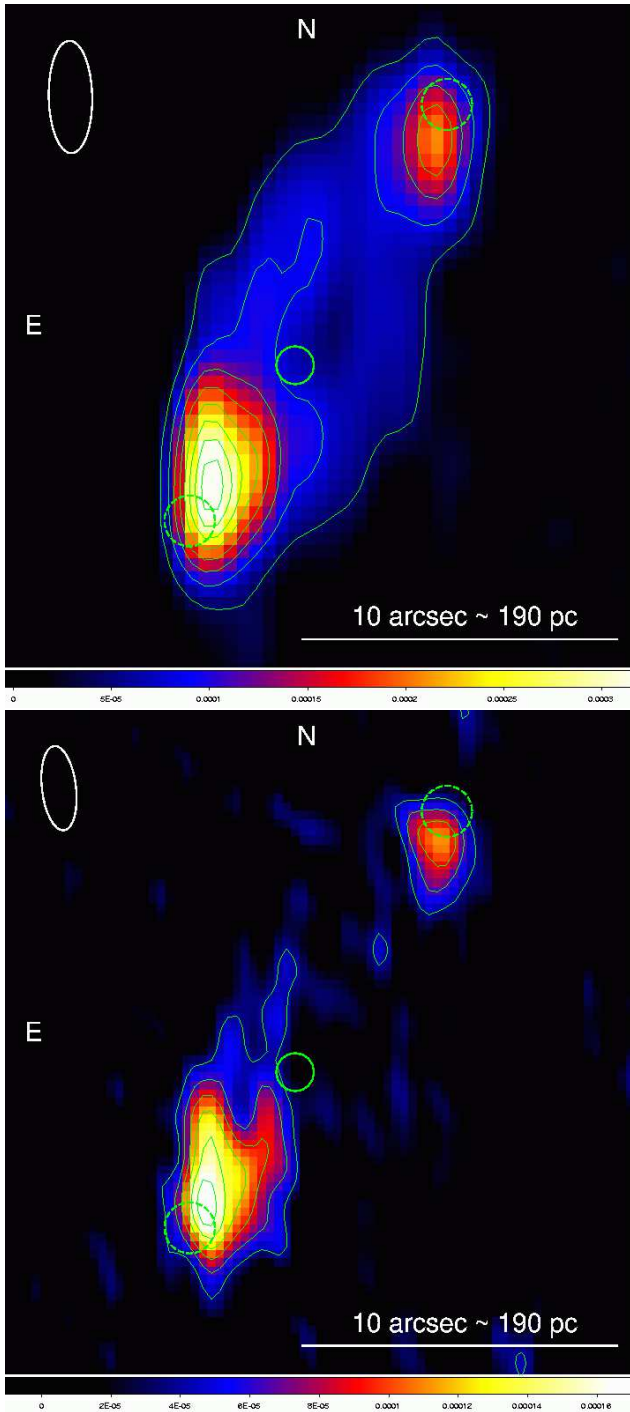


Figure 2. Top panel: ATCA map at 5.48 GHz, with intensity scale in Jy beam^{-1} . Contour intensity levels are $(0.40, 0.84, 1.29, 1.73, 2.17, 2.61, 3.06, 3.50) \times 10^{-4} \text{ Jy beam}^{-1}$. The rms noise level is $0.085 \times 10^{-4} \text{ Jy beam}^{-1}$. Overplotted green circles mark the positions of the X-ray core and hot spots ($0''.6$ radius for the core, $0''.8$ for the hot spots), from *Chandra*. Bottom panel: ATCA map at 9.02 GHz, with intensity scale in Jy beam^{-1} . Contour intensity levels are $(0.39, 0.65, 0.91, 1.17, 1.44, 1.70) \times 10^{-4} \text{ Jy beam}^{-1}$. The rms noise level is $0.135 \times 10^{-4} \text{ Jy beam}^{-1}$.

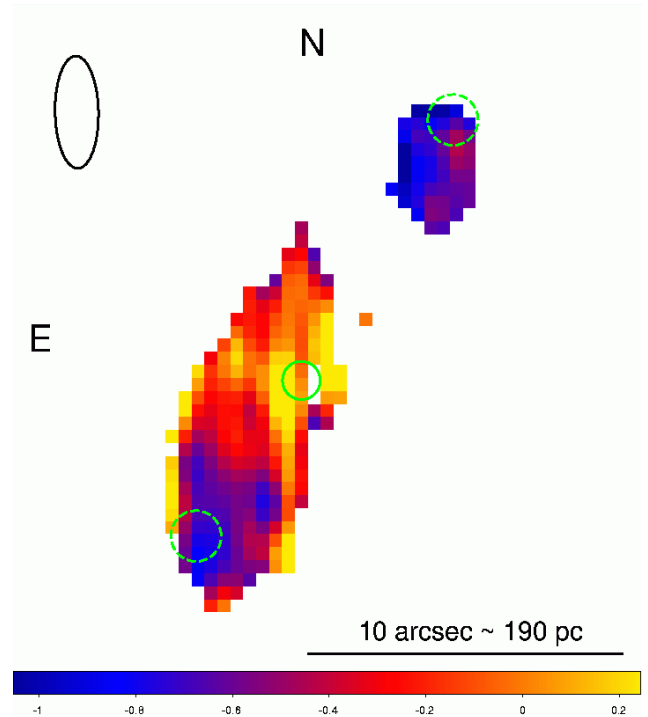


Figure 3. Map of the radio spectral index, inferred from the ratio of the 5.48 GHz and 9.02 GHz maps, where the latter has been tapered to the resolution of the former. Green circles mark the positions of the X-ray core and X-ray hot spots.

this system, quantifying the fraction of energy stored in relativistic electrons and in the X-ray emitting gas.

3 OBSERVATIONS

3.1 Radio observations

We observed S26 on 2009 August 6 and 7 with the Australia Telescope Compact Array (ATCA). Simultaneous 5.5 and 9 GHz observations were carried out with the Compact Array Broadband Backend (CABB); the bandwidth at each frequency is about 2 GHz. The array configuration was 6D, with minimum and maximum baselines of 77 and 5878 m, respectively. The total integration time on-source was 13.3 hours; the data for antenna 6 at 9 GHz were lost during part of the second observing session due to technical problems. B1934–638 was used as the primary calibrator, while our secondary calibrator was B2357–318.

We reduced and imaged the data with MIRIAD (Sault et al. 1995). After flagging bad data, the effective frequencies of the two bands are 5.48 and 9.02 GHz. We tried different values of Briggs’ robust weighting parameter (Briggs 1995); we found that a value of 0.0 provides a good balance between sidelobe suppression and sensitivity at both frequencies. Because of the wide bandwidths, we used the multi-frequency deconvolution algorithm MF-CLEAN (Sault & Wieringa 1994). The CLEANed, primary-beam-corrected images are shown in Figure 2; the angular resolutions are $3''.54 \times 1''.38$ (position angle 1.1°) and $2''.67 \times 1.08$ (position angle 6.8°) at 5.48 and 9.02 GHz, re-

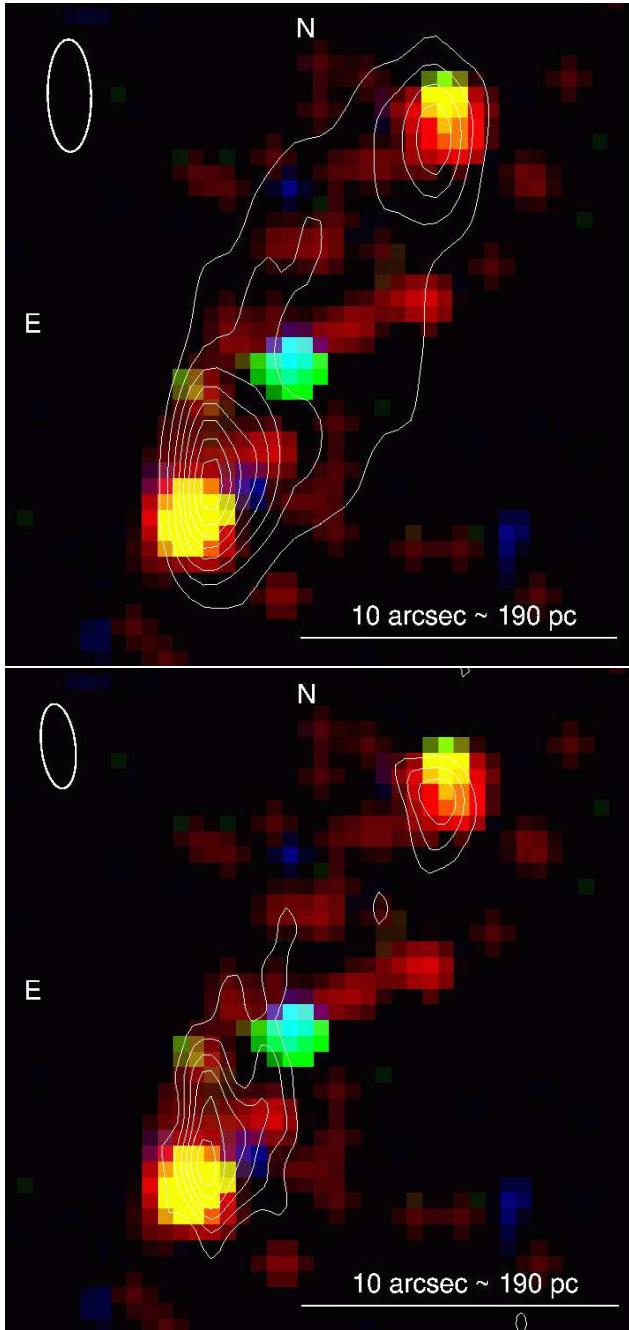


Figure 4. Top panel: *Chandra*/ACIS color map of S26 (smoothed with a $1''$ Gaussian core), with ATCA 5.48-GHz intensity contours. The colour coding is: red: 0.2–1 keV; green: 1–2 keV; blue: 2–8 keV. Contour intensity levels are as in Figure 2. Bottom panel: *Chandra*/ACIS X-ray colour map (same colour coding), with ATCA 9.02-GHz radio intensity contours superimposed. Contour intensity levels are as in Figure 2. Cf. Fig. 1 in PSM10, which overplots $H\alpha$ emission contours over the same *Chandra* image.

spectively. In the vicinity of the microquasar, the rms noise levels are $8.5\mu\text{Jy beam}^{-1}$ (5.48 GHz) and $13.5\mu\text{Jy beam}^{-1}$ (9.02 GHz). We estimate that the internal calibration uncertainty is ~ 2 per cent at both frequencies.

We also tapered the 9.02 GHz data so that the resolution and beam position angle matched those of the 5.48

GHz data. We created a two-point spectral index map (Figure 3), where the sign of the index is defined such that the specific flux $S_\nu \sim \nu^\alpha$. For the tapered 9.02 GHz data, we found that a robust weighting parameter of 0.5 provides the best compromise between residual sidelobe contamination and sensitivity to the low-surface-brightness extended emission that is clearly visible in the 5.5 GHz map.

3.2 X-ray observations

NGC 7793 was observed with *Chandra*/ACIS-S3 on 2003 September 6 (Obs ID 3954). The live time was 48.9 ks. We retrieved the data from the public archives (processed with ASCDVER=7.6.8), and analysed them with standard imaging and spectroscopic tools such as *psextract* in the data analysis system CIAO Version 4.0 (Fruscione et al. 2006). We modelled the X-ray spectra with XSPEC Version 12.0 (Arnaud 1996). Luckily, the roll angle of the *Chandra* observation was such that S26 was located rather close to the S3 aimpoint (less than $1'$ away), giving us a narrower point spread function.

4 MAIN RESULTS

4.1 Radio results

The most important new result of our ATCA study is that we have resolved the spatial structure of the radio-emitting nebula. Most of the emission comes from two radio hot spots and surrounding lobes, with a fainter but clearly identified cocoon encompassing them (Figure 2, top panel). This is the textbook structure (*e.g.*, Begelman et al. 1984) of FR II-type powerful radio galaxies (*e.g.*, Cygnus A: Carilli & Barthel 1996; Wilson et al. 2006). The radio structure is aligned with the jet axis suggested by the three X-ray sources, confirming this interpretation. The position of the northern radio hot spot is $\text{RA} = 23^{\text{h}}57^{\text{m}}59^{\text{s}}.58$, $\text{Dec} = -32^{\circ}33'13''.6$ (with an uncertainty of $\approx 0''.2$). The position of the southern hot spot is $\text{RA} = 23^{\text{h}}58^{\text{m}}00^{\text{s}}.15$, $\text{Dec} = -32^{\circ}33'25''.0$. Thus, the projected distance between the radio hot spots is $(13''.5 \pm 0''.3) \approx 250$ pc. We interpret the radio hot spots as the reverse shocks (Mach disks) at the ends of the jets.

At 5.5 GHz, the peak intensity in the southern lobe is ≈ 0.37 mJy beam^{-1} ; in the northern lobe, ≈ 0.21 mJy beam^{-1} ; the total flux in the lobes and cocoon is ≈ 2.1 mJy (Table 1), that is ≈ 3 times the luminosity of Cas A. From the untapered map at 9 GHz, we obtain a peak intensity in the southern lobe ≈ 0.19 mJy beam^{-1} ; in the northern lobe, ≈ 0.11 mJy beam^{-1} . The total flux at 9 GHz is ≈ 1.6 mJy (Table 1). The spectral index in the lobes is, on average, ≈ -0.7 to -0.6 ; it appears to be flatter (≈ -0.4 to 0) across most of the cocoon, and inverted (≈ 0 to 0.4) at the base of the jets, on either side of the X-ray/optical core (Figure 3). We estimate a 1σ uncertainty for α of ≈ 0.12 near the southern radio hot spot, ≈ 0.19 near the northern radio hot spot, and ≈ 0.5 – 0.6 in the rest of the cocoon, where the emission is much fainter. Thus, the existence of a complex spatial structure for the spectral index is at this stage still an intriguing speculation that has to be tested with deeper observations.

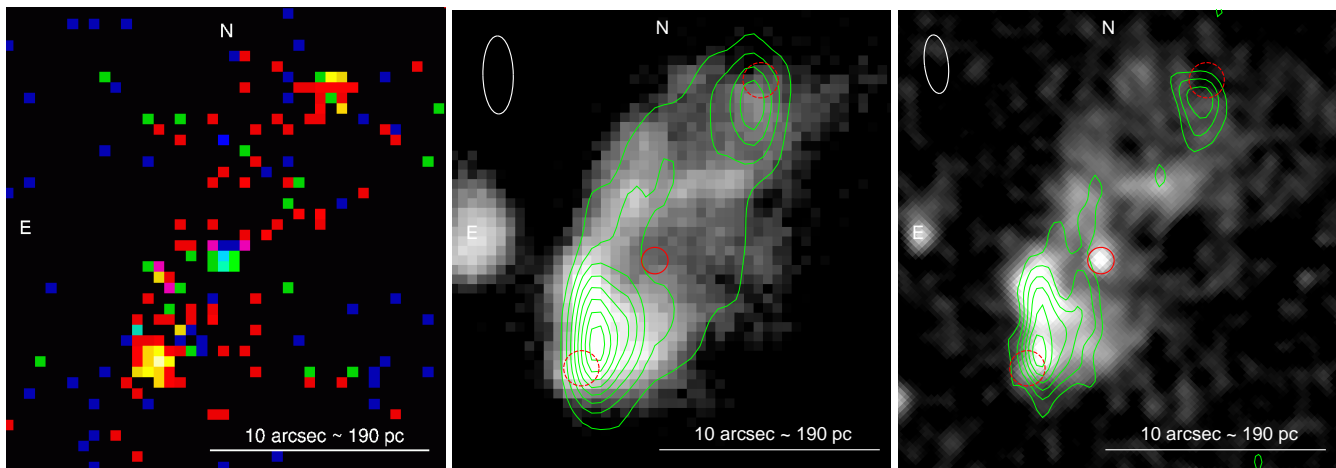


Figure 5. Left panel: unsmoothed *Chandra* color map, with the same colour coding as in Figure 4. Middle panel: greyscale, continuum-subtracted H α emission, with ATCA 5.5-GHz intensity contours. Red circles mark the positions of the X-ray core and hot spots ($0''.6$ radius for the core, $0''.8$ for the hot spots). The public-archive H α image was taken from the CTIO 1.5-m telescope on 2001 October 18. Right panel: greyscale, continuum-subtracted HeII λ 4686 emission, with ATCA 9.0-GHz intensity contours and X-ray core/hot spot positions. The image was taken with the FORS1 camera on the ESO Very Large Telescope on 2002 November 1; we smoothed it with a $0''.6$ Gaussian core. See PSM10 for a discussion of the bright optical core.

Structure	$S_{5.5}$ (mJy)	$S_{9.0}$ (mJy)
Total	2.1 ± 0.1	1.6 ± 0.1
S lobe	0.95 ± 0.05	0.80 ± 0.05
N lobe	0.45 ± 0.03	0.28 ± 0.03

Table 1. Observed radio fluxes for the whole nebula, and for the two lobes, from our ATCA observations. The 9.0-GHz fluxes are measured from the tapered map.

4.2 X-ray results

The key feature of this system is the aligned triplet of point-like sources (Figures 4, 5), which we interpret as the X-ray core and hot spots (Pakull & Grisé 2008). The X-ray core is located at RA = $23^h 57^m 59^s.94$, Dec = $-32^\circ 33' 20''.9$ (with an uncertainty of $\approx 0''.2$). It has a hard spectrum (power-law photon index $\Gamma = 1.4 \pm 0.6$), consistent with a BH in the low/hard state (Remillard & McClintock 2006), and an emitted luminosity $L_{0.3-8} \approx 6 \times 10^{36}$ erg s $^{-1}$ (Table 2 and Figure 6). The X-ray core coincides, within the astrometric uncertainties, with a point-like optical source with HeII λ 4686 emission (Figure 5). The 90% uncertainty circle of the ACIS-S3 absolute position has a radius of $0''.4^1$, and the uncertainty of the optical images is $\approx 0''.3$.

The two hot spots have a much softer spectrum (Figures 4, 6), and are well fitted (Table 3) by a 2-component *raymond-smith* thermal plasma model (Raymond & Smith 1977) with $kT_1 \approx 0.3$ keV and $kT_2 \approx 0.9$ keV, and negligible intrinsic absorption (Cash statistics = 10.4 over 13 dof for solar abundances; = 9.6 over 13 dof for 1/4-solar abundances). The emitted X-ray luminosities are $L_{0.3-8} \approx 5 \times 10^{36}$ erg s $^{-1}$ and $L_{0.3-8} \approx 11 \times 10^{36}$ erg s $^{-1}$ for the northern and southern hot spot, respectively (similar to the

ratio of radio luminosities). In general, a choice of low metal abundances give better fits than solar abundances, but the signal-to-noise is not high enough to constrain this parameter. Other, more complex thermal plasma models such as *mekal*, *vmekal*, *equil* and *nei* also give similar sets of best-fitting parameters; they all require at least two temperature components. However, the *sedov* thermal plasma model (Borkowski, Lyerly & Reynolds 2001) gives a good fit (Cash statistics = 11.9 over 15 dof for 1/4-solar abundances) with only one temperature component, at $kT \approx 0.52$ keV (Table 4); the ionization age (τ parameter) of the *sedov* model is consistent with the characteristic age multiplied by electron density in the S26 bubble. Given the small number of counts in the *Chandra* spectrum, none of the more complex thermal-plasma models can provide an improvement over the simpler *raymond-smith* model. Simple or broken power-law models do not give acceptable fits (Cash statistics = 25.5 over 15 dof); moreover, they would require an unphysically steep slope ($\Gamma \approx 6$) combined with high intrinsic column densities ($N_H \approx 5 \times 10^{21}$ cm $^{-2}$). We conclude that the hot spot spectra are not dominated by synchrotron or synchrotron self-Compton emission. We interpret them as optically-thin thermal plasma emission from hot, shocked gas, probably located between the reverse and forward shocks. The radius of the X-ray hot spots is $\lesssim 1''$. From the combined volume of the two hot spots and their emission measures (Table 3), we estimate a hot gas density $\gtrsim 1$ cm $^{-3}$ and a mass $\sim 10^{36}$ g (see also PSM10).

We also find faint X-ray emission projected over the surface of the cocoon (Figure 5), with slightly softer colours than the hot spots; however, the number of detected counts is too low for detailed temperature comparisons. A single-temperature bremsstrahlung fit suggests $kT = 0.5 \pm 0.1$ keV (Table 5 and Figure 7). It is also impossible to determine at this stage whether the X-ray emitting gas is filling the whole cocoon, or is confined to an outer shell. If the hot gas fills a

¹ <http://cxc.harvard.edu/cal/ASPECT/celmon/>

Parameter	Value
$N_{H,\text{Gal}}$	$1.2 \times 10^{20} \text{ cm}^{-2}$ (fixed)
Γ	$1.4^{+0.6}_{-0.6}$
K	$(4.3^{+2.1}_{-1.6}) \times 10^{-7}$
$f_{0.3-8}$	$(3.4^{+0.8}_{-0.8}) \times 10^{-15} \text{ erg cm}^{-2} \text{ s}^{-1}$
$L_{0.3-8}$	$(6.2^{+1.5}_{-1.5}) \times 10^{36} \text{ erg s}^{-1}$
C-statistic	4.56 (6 dof)

Table 2. Best-fitting spectral parameters for the X-ray emission from the core. The XSPEC model is $wabs_{\text{Gal}} * powerlaw$. Adding intrinsic absorption does not improve the fit. Errors are 90% confidence level for 1 interesting parameter. Here, and in the following tables, the line-of-sight column density to NGC 7793 is from Kalberla et al. (2005).

significant fraction of the cocoon, its characteristic density is $\sim 0.1 \text{ cm}^{-3}$ and the total mass $\sim 10^{37} \text{ g}$.

The position of the northern X-ray spot is RA = $23^{\text{h}}57^{\text{m}}59^{\text{s}}.56$, Dec = $-32^{\circ}33'12''.6$ (with an uncertainty of $\approx 0''.2$). The position of the southern X-ray spot is RA = $23^{\text{h}}58^{\text{m}}00^{\text{s}}.20$, Dec = $-32^{\circ}33'25''.7$. Therefore, the projected distance between the X-ray hot spots is $(15''.4 \pm 0''.3) \approx 290 \text{ pc}$, slightly larger than the projected distance between the radio hot spots; that is, each X-ray hot spot appears projected $\approx 15\text{--}20 \text{ pc}$ downstream from the corresponding radio hot spot. In fact, the X-ray and radio hot spot positions in the southern lobe coincide with two distinct brightness peaks in the optical images, particularly H α and V band (Figures 5, 8). This provides another argument in favor of two separate emission mechanisms for the radio and X-ray hot spots. The core is along the line of the hot spots, but not symmetrically located between them. It is projected $\approx 6''$ from the southern spot (which is about twice as luminous in every band) and $\approx 9''.5$ from the northern spot. This may perhaps be due to a higher density of the interstellar medium south of the core.

5 DISCUSSION

5.1 Energetics of the bubble

We have presented radio and X-ray results from our multi-band study of a powerful non-nuclear BH in NGC 7793, and of its surrounding shock-ionized cocoon (see PSM10 for a discussion of the evidence for shock ionization from the optical emission lines). The system was originally classified as a supernova remnant (Blair & Long 1997). In that scenario, Asvarov (2006) showed that an input energy $\approx 5 \times 10^{52} \text{ erg}$ was required to explain its size and radio luminosity, well beyond the energy that can be supplied by an individual supernova. Based on the clear radio and X-ray evidence for a collimated jet pair (lobes, hot spots), PSM10 showed that such a large amount of energy has been supplied by the BH over the lifetime of the bubble (characteristic age $\approx 2 \times 10^5 \text{ yr}$). The core is seen as a faint point-like X-ray source, consistent with a stellar-mass BH in the low/hard state, and a point-like optical source, consistent with an OB donor star (possibly a

Parameter	Value
$N_{H,\text{Gal}}$	$1.2 \times 10^{20} \text{ cm}^{-2}$ (fixed)
N_H	$< 1.0 \times 10^{21} \text{ cm}^{-2}$
Z	1 (fixed)
kT_1	$0.26^{+0.05}_{-0.08} \text{ keV}$
N_1	$(2.3^{+2.9}_{-0.6}) \times 10^{-6}$
kT_2	$0.96^{+0.31}_{-0.17} \text{ keV}$
N_2	$(1.9^{+0.7}_{-0.7}) \times 10^{-6}$
$f_{0.3-8}$	$(8.8^{+0.9}_{-0.9}) \times 10^{-15} \text{ erg cm}^{-2} \text{ s}^{-1}$
$L_{0.3-8}$	$(1.7^{+1.2}_{-0.3}) \times 10^{37} \text{ erg s}^{-1}$
EM(0.26 keV)	$(4.2^{+5.3}_{-1.1}) \times 10^{59} \text{ cm}^{-3}$
EM(0.96 keV)	$(3.5^{+1.3}_{-1.3}) \times 10^{59} \text{ cm}^{-3}$
C-statistic	10.35 (13 dof)

Parameter	Value
$N_{H,\text{Gal}}$	$1.2 \times 10^{20} \text{ cm}^{-2}$ (fixed)
N_H	$< 1.1 \times 10^{21} \text{ cm}^{-2}$
Z	0.25 (fixed)
kT_1	$0.29^{+0.08}_{-0.11} \text{ keV}$
N_1	$(7.3^{+12.2}_{-3.1}) \times 10^{-6}$
kT_2	$0.90^{+0.32}_{-0.16} \text{ keV}$
N_2	$(4.9^{+9.2}_{-1.9}) \times 10^{-6}$
$f_{0.3-8}$	$(9.1^{+0.9}_{-0.9}) \times 10^{-15} \text{ erg cm}^{-2} \text{ s}^{-1}$
$L_{0.3-8}$	$(1.8^{+1.2}_{-0.3}) \times 10^{37} \text{ erg s}^{-1}$
EM(0.29 keV)	$(13.3^{+22.2}_{-5.6}) \times 10^{59} \text{ cm}^{-3}$
EM(0.90 keV)	$(8.9^{+16.7}_{-3.5}) \times 10^{59} \text{ cm}^{-3}$
C-statistic	9.55 (13 dof)

Table 3. Best-fitting spectral parameters for the (combined) hot spot X-ray emission, assuming solar and 1/4-solar abundances. The XSPEC model is $wabs_{\text{Gal}} * wabs * (ray + ray)$. Errors are 90% confidence level for 1 interesting parameter.

Wolf-Rayet: PSM10). It is undetected in the radio bands, to a 3σ upper limit $\approx 0.03 \text{ mJy}$. This is unsurprising; if the BH lies in the fundamental plane (Merloni, Heinz & Di Matteo 2003; Körding, Falcke & Corbel 2006) with a mass $\sim 10M_{\odot}$, we expect a core radio flux $\sim 0.01 \mu\text{Jy}$ ($\nu L_{\nu} \sim 10^{30} \text{ erg s}^{-1}$), like from a common-or-garden low/hard state microquasar at a distance of 3.9 Mpc. On the other hand, the impact of this BH onto the surrounding interstellar medium is all but common. The simplest explanation is that the core is currently in a low/hard state, three or four orders of magnitude fainter than its long-term average power. In that same canonical state, the steady jet power $\mathcal{P} \propto L_X^{0.5}$ (Fender, Belloni & Gallo 2004; Malzac, Merloni & Fabian 2004; Fender, Gallo & Jonker 2003). The normalization of this relation has an uncertainty of almost two orders of magnitude, but is constrained enough to suggest $10^{36} \text{ erg s}^{-1} \lesssim \mathcal{P} \lesssim 10^{38} \text{ erg s}^{-1}$, also much lower than the inferred long-term average. However, there may be alternative explanations for the apparent faintness of the core. Perhaps the observed X-ray luminosity is a severe underestimate of the

Parameter	Value
$N_{H,\text{Gal}}$	$1.2 \times 10^{20} \text{ cm}^{-2}$ (fixed)
N_H	$< 2.5 \times 10^{21} \text{ cm}^{-2}$
Z	0.25 (fixed)
kT	$0.78^{+0.07}_{-0.16} \text{ keV}$
N	$(8.4^{+8.7}_{-1.4}) \times 10^{-6}$
C-statistic	28.9 (15 dof)
$N_{H,\text{Gal}}$	$1.2 \times 10^{20} \text{ cm}^{-2}$ (fixed)
N_H	0 (fixed)
Z	0.25 (fixed)
kT_a	$0.52^{+0.19}_{-0.13} \text{ keV}$
kT_b	kT_a (fixed)
τ	$(1.9^{+11.1}_{-1.4}) \times 10^{12} \text{ s cm}^{-3}$
N_{sed}	$(8.7^{+2.8}_{-2.8}) \times 10^{-6}$
$f_{0.3-8}$	$(9.0^{+1.6}_{-1.8}) \times 10^{-15} \text{ erg cm}^{-2} \text{ s}^{-1}$
$L_{0.3-8}$	$(1.8^{+0.3}_{-0.3}) \times 10^{37} \text{ erg s}^{-1}$
EM	$(15.9^{+5.1}_{-5.1}) \times 10^{59} \text{ cm}^{-3}$
C-statistic	11.88 (15 dof)

Table 4. Alternative spectral models for the combined hot spot X-ray emission. A single-temperature $wabs_{\text{Gal}}*wabs*ray$ model does not produce acceptable fits. However, a single-temperature $wabs_{\text{Gal}}*wabs*sedov$ model results in a fit as good as those with two-temperature $raymond-smith$ models (Table 3). Errors are 90% confidence level for 1 interesting parameter.

true X-ray luminosity, if most of the direct emission is absorbed and/or beamed away from our line of sight (as it has been suggested for SS 433: Medvedev & Fabrika 2010) and we are only seeing a scattered component. Or perhaps the system is not in the canonical low/hard state, but in some other unclassified state with $\mathcal{P} \gg L_X$.

The faint core is in stark contrast with the large, bright nebula, visible in all bands with a similar size and shape (Figure 5), and a conservatively estimated volume $\approx 10^{62} \text{ cm}^{-3}$, assuming a prolate spheroid with a major axis $\approx 280 \text{ pc}$ and minor axes $\approx 130 \text{ pc}$ (based on the projected distance between the hot spots along the major axis, and the width of the radio nebula at 5.5 GHz in the transverse direction). In fact, H α images (PSM10) may suggest an even larger size, $\approx 340 \times 170 \text{ pc}$. Thus, the volume-averaged shell radius $R_s \approx 100 \text{ pc}$. Its characteristic size is an order of magnitude larger than the jet driven bubble around Cyg X-1, which has an estimated jet power $\sim 10^{37} \text{ erg s}^{-1}$ (Russell et al. 2007). It is a factor of two larger (allowing for distance uncertainties) than the radius of the SS433/W50 nebula, with an estimated jet power $\sim 10^{39} \text{ erg s}^{-1}$ (Medvedev & Fabrika 2010; Fabrika 2004; Marshall, Canizares & Schulz 2002).

PSM10 determined a mechanical power $\mathcal{P} \approx 5 \times 10^{40} \text{ erg s}^{-1}$ for S26, using the well-known self-similar solution to the conservation of mass, momentum and energy equations (Equations 17–22 in Weaver et al. 1977), in which the radius of the swept-up shell $R_s \approx 0.76 \mathcal{P}^{1/5} t^{3/5} \rho_0^{-1/5}$. They measured the expansion velocity from the half-width at zero-

Parameter	Value
$N_{H,\text{Gal}}$	$1.2 \times 10^{20} \text{ cm}^{-2}$ (fixed)
Z	0.25 (fixed)
kT_1	0.29 keV (fixed)
N_1	$(3.5^{+2.1}_{-1.8}) \times 10^{-6}$
kT_2	0.90 keV (fixed)
N_2	$(2.1^{+1.6}_{-1.3}) \times 10^{-6}$
$f_{0.3-8}$	$(4.2^{+0.6}_{-0.6}) \times 10^{-15} \text{ erg cm}^{-2} \text{ s}^{-1}$
$L_{0.3-8}$	$(7.6^{+1.1}_{-1.1}) \times 10^{36} \text{ erg s}^{-1}$
EM(0.26 keV)	$(6.4^{+3.8}_{-3.3}) \times 10^{59} \text{ cm}^{-3}$
EM(0.96 keV)	$(3.8^{+2.9}_{-2.4}) \times 10^{59} \text{ cm}^{-3}$
C-statistic	11.28 (17 dof)
$N_{H,\text{Gal}}$	$1.2 \times 10^{20} \text{ cm}^{-2}$ (fixed)
kT_{br}	$0.47^{+0.15}_{-0.13} \text{ keV}$
K_{br}	$(7.5^{+5.9}_{-3.2}) \times 10^{-6}$
$f_{0.3-8}$	$(5.1^{+0.8}_{-0.8}) \times 10^{-15} \text{ erg cm}^{-2} \text{ s}^{-1}$
$L_{0.3-8}$	$(9.3^{+1.5}_{-1.5}) \times 10^{36} \text{ erg s}^{-1}$
EM	$(4.5^{+3.5}_{-1.9}) \times 10^{60} \text{ cm}^{-3}$
C-statistic	9.77 (17 dof)

Table 5. Best-fitting spectral parameters for the X-ray emission from the cocoon (not including the hot spots). The XSPEC models are $wabs_{\text{Gal}}*ray$ and $wabs_{\text{Gal}}*brems$. Adding intrinsic absorption does not improve the fit. Errors are 90% confidence level for 1 interesting parameter.

intensity of the optical emission lines ($v \approx 250 \text{ km s}^{-1}$) and from shock-ionization models of the HeII $\lambda 4686/\text{H}\beta$ flux ratio ($v \approx 275 \text{ km s}^{-1}$). This implies a characteristic age $t = (3R_s)/(5v_{\text{exp}}) \approx 2 \times 10^5 \text{ yr}$. The hydrogen number density of the interstellar medium into which the bubble expands was estimated as $n_0 \approx 0.7 \text{ cm}^{-3}$ (PSM10), from a comparison of the observed H α emission with the intensity of a fully radiative shock (Dopita & Sutherland 1996; Pakull et al. 2006); this corresponds to a mass density $\rho_0 \approx \mu m_p n_0 \approx 1.6 \times 10^{-24} \text{ g cm}^{-3}$ (taking the mean atomic weight $\mu = 1.38$). The swept-up mass in the expanding shell is $(4\pi/3)\rho R_s^3 \approx 2 \times 10^{38} \text{ g}$, carrying a kinetic energy $\simeq (15/77)\mathcal{P}t \approx 6 \times 10^{52} \text{ erg}$. The energy content of the thermal gas between the reverse shock and the swept-up shell is $E = (5/11)\mathcal{P}t \approx 10^{53} \text{ erg}$.

The only shock-ionized nebulae of comparable size and energy content in the local universe are those around ULXs such as Holmberg IX X-1, NGC 1313 X-2, IC 342 X-1 (Pakull & Mirioni 2002; Pakull & Grisé 2008; Ramsey et al. 2006; Feng & Kaaret 2008). One difference is that, unlike all previously known ULX bubbles, S26 has clear evidence of collimated jets. We do not know the relative distribution of mechanical power between the collimated jets and perhaps a more spherically symmetric wind (for example an accretion disk wind); however, the elongated structure of the nebula and the presence of bright lobes and hot spots suggests that the jet carries most of the power. Another difference is that

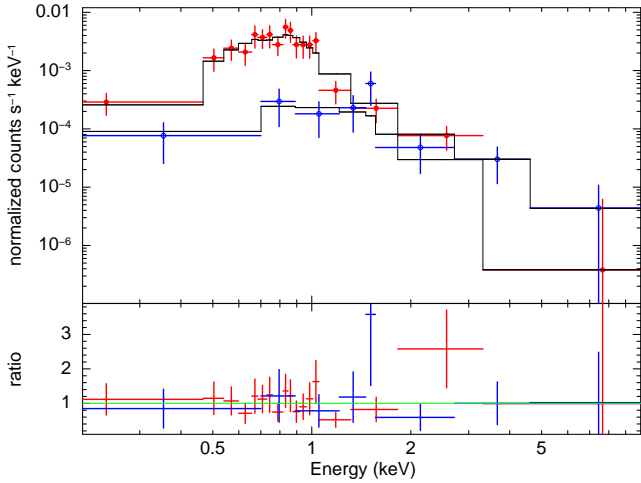


Figure 6. *Chandra*/ACIS spectra of the combined hot spot emission (red datapoints) and core emission (blue datapoints), fitted with a single-temperature *sedov* thermal-plasma model and with a power-law model, respectively. See Tables 2, 3, 4 for the best-fitting parameters. The *sedov* model fit illustrated here is statistically equivalent to the two-temperature *raymond-smith* model fit illustrated in Fig. 2 of PSM10.

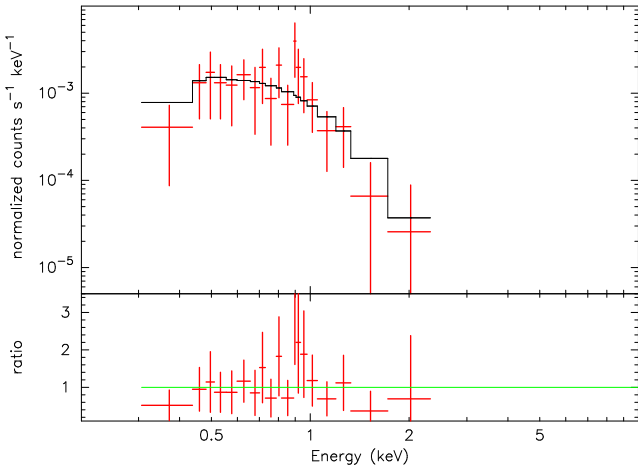


Figure 7. *Chandra*/ACIS spectrum of the cocoon emission, fitted with a ≈ 0.5 keV bremsstrahlung model. See Table 5 for the best-fitting parameters.

in ULX bubbles, the central BH is (by definition) X-ray luminous, with an apparent X-ray luminosity $\sim 10^{40}$ erg s^{-1} , similar to the mechanical power. S26 may be an example of ULX bubble where the central BH is currently in a low and/or jet-dominated state. In that respect, S26 is analogous to (but two orders of magnitude more energetic than) the shock-ionized bubble around the very massive but only moderately luminous non-nuclear BH IC 10 X-1 (Prestwich et al. 2007).

5.2 Synchrotron and thermal plasma emission

The detection of a radio cocoon with bright radio hot spots shows that some of the input mechanical power goes into synchrotron-emitting, relativistic electrons. As expected, the radio spectrum is steep in the lobes and flat or inverted near

the position of the core (Figure 3); this may be evidence of recent or continuing ejection activity (although the core itself is undetected in the radio). In addition, there is radio emission from the cocoon region outside the lobes, with a specific flux ≈ 0.7 mJy at 5.5 GHz. There is circumstantial evidence that this emission has a rather flat spectrum, certainly flatter than in the lobes (Figure 3). This is difficult to reconcile with a scenario where the synchrotron-emitting electrons in the whole cocoon are backflowing from the lobes. In that case, the spectral index in the rest of the cocoon would be even steeper—as we see for example in Cygnus A (Carilli & Barthel 1996). We suggest that the extended radio emission in the cocoon outside the lobes may have a significant contribution from (flat-spectrum) free-free emission, from the same thermal gas responsible for the optical recombination lines. For the characteristic temperature $\approx 3 \times 10^4$ K estimated by PSM10, the ratio of the $H\beta$ and free-free radio emissivity is $j_{H\beta}/j_{5.5\text{GHz}} \approx 2 \times 10^{-10}$ erg cm^{-2} s^{-1} Jy^{-1} (Caplan & Deharveng 1986, their Appendix A). The $H\beta$ luminosity of S26 is $\approx 10^{38}$ erg s^{-1} (PSM10): thus, we expect a free-free radio flux ≈ 0.3 mJy at 5.5 GHz. This is negligible in the lobes, compared with the synchrotron component, but may be significant in the region outside the lobes, and may explain the rather flat spectral index there.

What fraction of the mechanical power is transferred to relativistic electrons? If we combine the self-similar model of cocoon expansion with the standard synchrotron emissivity, in the minimum-energy approximation, assuming a spectral index $\alpha = -0.7$, we obtain (Appendix A):

$$S_\nu \approx 82 (1+k)^{-1} \eta^{1.85} \mathcal{P}_{39}^{1.34} t_5^{0.32} n_1^{0.51} d_1^{-2} \nu_5^{-0.7} \text{ mJy}, \quad (1)$$

where η is the fraction of the total energy density contained in all relativistic species (electrons, protons and nuclei) plus magnetic field, $(1+k)^{-1}$ is the fraction of relativistic particle energy carried by the synchrotron-emitting electrons alone, \mathcal{P}_{39} is the jet power in units of 10^{39} erg s^{-1} , t_5 is the source age in units of 10^5 yr, n_1 is the interstellar number density in cm^{-3} , d is the source distance in Mpc, and ν_5 the observed frequency in units of 5 GHz. A specific flux a few times higher is expected if we assume $\alpha = -0.5$ (Appendix A).

If we assume that all the jet power is transferred to the relativistic electrons (that is, if we put $k = 0$ and $\eta = 1$), Equation (1) grossly overestimates the radio emission, for the measured jet power and distance of S26. (Or, conversely, the observed radio flux would lead us to underestimate the jet power if we did not know it independently). This tells us that $(1+k)^{-1} \times \eta^{1.85} \sim 10^{-3}$. We cannot separately determine k and η from this simple model, but for plausible values of $k \sim 10$ –100 found in cosmic rays, we estimate that the fraction $(1+k)^{-1} \times \eta$ of the total injected mechanical power carried by the relativistic electrons is \sim a few 10^{-3} . The rest of the energy is given to protons, nuclei and non-relativistic electrons, and is used for heating and inflating the bubble, accelerating the shell of swept-up interstellar medium to the expansion speed ≈ 250 km s^{-1} .

The X-ray emission from the hot spots and cocoon provides another clue to understand the energy budget. In radio galaxies, X-ray hot spots are usually interpreted either as direct synchrotron, or synchrotron self-Compton emission (Harris & Krawczynski 2002; Hardcastle et al. 2004), from the same population of electrons responsible for the radio hot spots, which are accelerated at the reverse shock. For

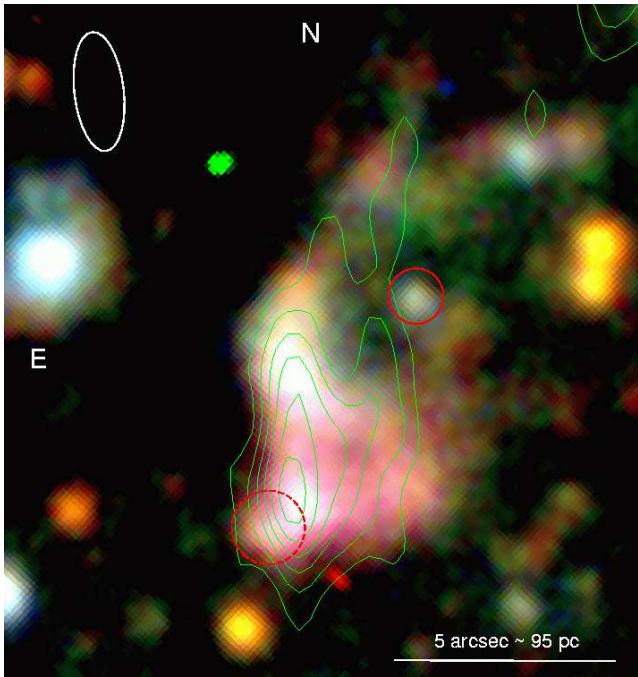


Figure 8. Close-up view of the southern lobe: true-colour image in the B, V, R bands, taken by Dr. Jifeng Liu with the Baade *Magellan* telescope on 2009 August 28 (exposure time: 200 s per filter). The ATCA 9.02-GHz intensity contours are overplotted in green; the red circles mark the position of the X-ray core and southern hot spot. The point-like optical core has a brightness $B \approx 23$ mag, $M_B \approx -5$ mag (PSM10).

S26, we estimate from *Chandra* a specific flux $\approx 10^{-14}$ erg $\text{cm}^{-2} \text{s}^{-2} \text{keV}^{-1}$ at 1 keV from both hot spots, corresponding to $\approx 4 \times 10^{-32}$ erg $\text{cm}^{-2} \text{s}^{-2} \text{Hz}^{-1}$. The combined radio emission from the radio hot spots is ≈ 1 mJy $\approx 10^{-26}$ erg $\text{cm}^{-2} \text{s}^{-2} \text{Hz}^{-1}$ at 5.5 GHz. If we extrapolate the radio flux as a straight power law, $S_\nu \sim \nu^{-0.7}$, we would also expect $\approx 4 \times 10^{-32}$ erg $\text{cm}^{-2} \text{s}^{-2} \text{Hz}^{-1}$ at 1 keV. This of course requires a continuous acceleration of the most energetic electrons, so that there is no spectral break from the radio to the X-ray bands. So, in principle, the X-ray to radio flux ratio is consistent with a simple synchrotron component. However, the X-ray spectrum tells a different story. Its shape and slope are not consistent with either synchrotron or inverse-Compton power-law models, even accounting for the low number of counts. We showed (Section 4 and Figure 6) that the X-ray emission from the hot spots, with its peak at ~ 0.6 – 0.9 keV and its sharp drop above ≈ 1 keV, is most likely due to hot thermal plasma with a range of temperatures up to ≈ 0.9 keV. We also showed that the X-ray hot spots are located $\approx 1''$ further away from the core than the radio hot spots. This is a second argument in support of our claim that X-ray and radio hot spots are due to different physical processes.

It is still not clear what is heating at least part of the X-ray emitting gas to such high temperatures, particularly at the hot spots. We suggest two alternative scenarios. The first scenario is that the X-ray emitting gas is the shocked interstellar medium, heated by the bow shock (advancing at a speed v_{bs}) to a temperature $kT = (3/16)\mu m_p v_{\text{bs}}^2$. In this case, the X-ray hot spots mark the position of the bow shock

and the radio hot spots that of the reverse shock into the ejecta. To produce temperatures ≈ 0.9 keV (as required by our fits with *raymond-smith* and most other thermal plasma models in XSPEC), the bow shock velocity (that is, the expansion velocity along the major axis) would have to be ≈ 900 km s^{-1} , almost 4 times higher than the expansion velocity measured by PSM10 from the width of the optical lines. However, their slit position was almost parallel to the minor axis and did not include the hot spots; moreover, the viewing angle of the major axis is still unknown. Thus, we still do not know at what speed the jet heads are advancing into the interstellar medium. Besides, we noted in Section 4.1 that a *sedov* model gives a good fit of the hot spot emission with thermal plasma temperatures as low as ≈ 0.5 keV, requiring a more plausible shock velocity ≈ 300 km s^{-1} . To sum up, we cannot yet rule out the fast bow shock scenario for S26. An example of an X-ray-emitting bow shock located ahead of the radio-emitting lobes can be seen in the nearest radio galaxy, Cen A (Kraft et al. 2007). An alternative scenario, considered more likely by PSM10, is that the bow shock is not advancing fast enough to produce the X-ray emitting gas, and the shocked interstellar gas between the bow shock and the contact discontinuity has already cooled and collapsed to a thin, dense shell. In this case, the X-ray emitting gas is located between the reverse shock and the swept-up outer shell, and is heated by the shocked ejecta via thermal conduction. Most of the mass in the hot region must come from mass-loading of denser interstellar clouds during the bubble expansion, and from the evaporation of part of the swept-up shell of interstellar medium, and its mixing with the lower-density, hotter jet material.

The physical size of the X-ray hot spots is $\lesssim 20$ pc in radius, and the projected size of the whole bubble is $\approx 300 \times 150$ pc. From the estimated emission measures (Tables 3–5), we infer a mass of X-ray emitting gas \sim a few $100M_\odot$ in the hot spots (see also PSM10) and \sim a few $1000M_\odot$ in the cocoon (assuming a filling factor ~ 1). These values are several orders of magnitude higher than the mass that could have been carried out by the BH jet and winds over the source lifetime. But the mass of X-ray emitting gas is an order of magnitude less than the total mass of the swept-up interstellar medium; that is, the swept-up shell is not significantly depleted by evaporation into the hot region, in agreement with the self-similar approximation of Weaver et al. (1977). From the estimated mass and fitted X-ray temperatures, we conclude that the X-ray-emitting gas contains a thermal energy $\sim 10^{51}$ erg (hot spots) and $\sim 10^{52}$ erg (whole cocoon). And we showed earlier that the total thermal energy $\sim 10^{53}$ erg and the energy carried by the synchrotron-emitting relativistic electrons \sim a few 10^{50} erg. The cooling timescale of the X-ray emitting gas in the cocoon is $\sim 10^7$ yr, 100 times longer than the age of the source. This is consistent with an emitted X-ray luminosity $\sim 10^{37}$ erg s^{-1} even though power may have been transferred from the jet to the ~ 0.3 – 1 keV component of the gas at an average rate $\sim 10^{39}$ erg s^{-1} . By analogy with other shock-heated bubbles, we suggest that there may be even hotter but much less dense gas components, especially near the hot spots, whose hard X-ray emission would be too faint to be detectable in the 50-ks *Chandra* observation.

6 CONCLUSIONS

We have carried out a multiband study of the shock-ionized bubble S26 in NGC 7793, which looks like a long-sought analogue of the Galactic jet source SS 433/W50 but on an even grander scale (projected size $\approx 300 \times 150$ pc). We showed that its structure is a scaled-down version of powerful FR II radio galaxies, with a core, radio lobes, X-ray hot spots and cocoon. It is the first time that all these elements have been found in a non-nuclear BH. We showed that the radio and X-ray hot spots are not spatially coincident: the X-ray hot spots are ≈ 20 pc further out than the peak of the radio intensity in the lobes. This suggests that X-ray and radio emission come from different populations of radiating particles. Based on our *Chandra* spectral analysis, we argued that the X-ray emission from the hot spots is most likely thermal. From the ATCA data, we showed that the radio emission from the lobes has a steep spectrum, consistent with optically-thin synchrotron emission. Over the rest of cocoon, the radio spectrum is flatter, suggesting an additional contribution from free-free emission; this is consistent with what we would expect from the measured $H\beta$ line emission. A point-like radio core is not detected, but the radio spectrum is flat or inverted in the proximity of the X-ray/optical core position; this may be interpreted as a more recent ejection. However, deeper ATCA observations are needed (and scheduled) to test this suggestion.

The total particle energy in the bubble is $\sim 10^{53}$ erg. Based on the measured radio flux and size of the bubble, and using standard equipartition relations for microquasar lobes, we estimated that the energy carried by the synchrotron-emitting relativistic electrons is a few 100 times less than the energy stored in protons, nuclei and non-relativistic electrons; non-relativistic particles provide most of the pressure to inflate the bubble. This system can give us important clues on how BHs at near-Eddington accretion rates transfer energy to the surrounding medium. The size and total energy content of the bubble are comparable to those found in some ULXs. However, here the core appears to be currently X-ray faint (and was so also during the *Einstein* and *ROSAT* observations), while the jet is carrying a long-term-average power $\sim 10^{40}$ erg s^{-1} (PSM10). We do not have any information on the long-term-average X-ray luminosity of the core, so we cannot exclude that it is similar to the mechanical power. If the BH in S26 is of stellar origin, its super-Eddington jet power may force us to rethink the “canonical” scheme of BH accretion states. In Galactic BH transients, a collimated jet is present at accretion rates \lesssim a few percent of the Eddington rate (low/hard state). At higher accretion rates (~ 0.05 – 0.5 Eddington), the accretion flow usually collapses to a geometrically-thin, radiatively-efficient thermal disk, and the jet is quenched. At even higher accretion rates (above Eddington), high X-ray luminosity and powerful mass-loaded outflows may coexist, but it is not known whether there can also be steady, collimated jets, and what their power is compared with the radiative power. S26 suggests that there can be collimated jets, and they may even dominate over the radiative output. The same scenario has been suggested for some powerful FR II radio galaxies and quasars (Punsly 2007; Ito et al. 2008).

ACKNOWLEDGMENTS

We thank: Tasso Tzioumis for his assistance when we prepared the ATCA observations; Jifeng Liu for his taking of an optical image for us, using his own time at the Magellan telescope; Mike Dopita for comments and for his taking of an optical spectrum for us, from his own time at the ANU 2.3m telescope; Geoff Bicknell, Fabien Grisé, JingFang Hao, Albert Kong, Zdenka Kuncic and Kinwah Wu for comments. RS acknowledges hospitality at the National Tsing Hua University (Taiwan), at the Institute for High Energy Physics (Beijing), and at the University of Sydney, during part of this work. The Australia Telescope is funded by the Commonwealth of Australia for operation as a National Facility managed by CSIRO.

REFERENCES

- Arnaud, K. A. 1996, *Astronomical Data Analysis Software and Systems V*, eds. G. Jacoby and J. Barnes, ASP Conf. Series volume 101, 17
- Asvarov, A. I. 2006, *A&A*, 459, 519
- Begelman, M. C., Hatchett, S. P., McKee, C. F., Sarazin, C. L., & Arons, J. 1980, *ApJ*, 238, 722
- Begelman, M. C., Blandford, R. D., & Rees, M. J. 1984, *RevModPhys*, 56, 255
- Bicknell G. V., 2005, *Lecture Notes on High Energy Astrophysics* (Australian National University, Canberra), <http://www.mso.anu.edu.au/~geoff/HEA/HEA.html>
- Blair, W. P., & Long, K. S. 1997, *ApJS*, 108, 261
- Blandford, R. D., & Rees, M. J. 1974, *MNRAS*, 169, 395
- Blundell K. M., Rawlings S., 2000, *AJ*, 119, 1111
- Borkowski, K. J., Lyerly, W. J., & Reynolds, S. P. 2001, *ApJ*, 548, 820
- Briggs, D. S. 1995, Ph.D. Thesis, New Mexico Institute of Mining and Technology, Socorro (New Mexico); available online from the NRAO Library, <http://www.aoc.nrao.edu/dissertations/dbriggs/>
- Caplan, J., & Deharveng, L. 1986, *A&A*, 155, 297
- Carilli, C. L., & Barthel, P. D. 1996, *A&ARv*, 7, 1
- Cavagnolo, K. W., McNamara, B. R., Nulsen, P. E. J., Carilli, C. L., Jones, C., & Birzan, L. 2010, *ApJ*, in press (arXiv:1006.5699)
- Corbel, S., Fender, R. P., Tzioumis, A. K., Tomsick, J. A., Orosz, J. A., Miller, J. M., Wijnands, R., & Kaaret, P. 2002, *Science*, 298, 196
- Corbel, S., Kaaret, P., Fender, R. P., Tzioumis, A. K., Tomsick, J. A., Orosz, J. A. 2005, *ApJ*, 632, 504
- Dopita, M. A., Sutherland, R. S. 1996, *ApJS*, 102, 161
- Fabrika, S. 2004, *ASPRv*, 12, 1
- Fender, R. P., Belloni, T. M., & Gallo, E. 2004, *MNRAS*, 355, 1105
- Fender, R. P., Gallo, E., & Jonker, P. G. 2003, *MNRAS*, 343, L99
- Feng, H., & Kaaret, P. 2008, *ApJ*, 675, 1067
- Fomalont, E. B., Geldzahler, B. J., & Bradshaw, C. F. 2001, *ApJ*, 558, 283
- Fruscione, A., et al. 2006, *proc. of SPIE*, 6270, 60
- Gallo, E., Fender, R., Kaiser, C., Russell, D., Morganti, R., Oosterloo, T., & Heinz, S. 2005, *Nature*, 436, 819
- Grisé, F., Pakull, M. W., Soria, R., Motch, C., Smith, I. A., Ryder, S. D., & Böttcher, M. 2008, *A&A*, 486, 151

- Hao, J. F., & Zhang, S. N. 2009, *ApJ*, 702, 1648
- Hardcastle, M. J., Harris, D. E., Worrall, D. M., & Birkinshaw, M. 2004, *ApJ*, 612, 729
- Harris, D. E., & Krawczynski, H. 2002, *ApJ*, 565, 244
- Heinz, S. 2002, *A&A*, 338, L40
- Heinz, S. 2008, *AIP Conf. Proc.*, 1010, 40
- Ito, H., Kino, M., Kawakatu, N., Isobe, N., & Yamada, S. 2008, *ApJ*, 685, 828
- Kaiser, C. R., & Alexander, P. 1997, *MNRAS*, 286, 215
- Kaiser, C. R., Gunn, K. F., Brocksopp, C., & Sokolowski, J. L. 2004, *ApJ*, 612, 332
- Kalberla, P. M. W., Burton, W. B., Hartmann, D., Arnal, E. M., Bajaja, E., Morras, R., & Pöppel, W. G. L. 2005, *A&A*, 440, 775
- Karachentsev, I. D., et al. 2003, *A&A*, 404, 93
- Körding, E., Falcke, H., & Corbel, S. 2006, *A&A*, 456, 439
- Kraft, R. P., et al. 2007, *ApJ*, 665, 1129
- Lang, C. C., Kaaret, P., Corbel, S., & Mercer, A. 2007, *ApJ*, 666, 79
- Leahy, J. P., & Gizani, N. 2001, *ApJ*, 555, 709
- Malzac, J., Merloni, A., & Fabian, A. C. 2004, *MNRAS*, 351, 253
- Marshall, H. L., Canizares, C. R., & Schulz, N. S. 2002, *ApJ*, 564, 941
- Martí, J., Pérez-Ramírez, D., Garrido, J. L., Luque-Escamilla, P., & Paredes, J. M. 2005, *A&A*, 439, 279
- Medvedev, A., & Fabrika, S. 2010, *MNRAS*, 402, 479
- Merloni, A., Heinz, S., & di Matteo, T. 2003, *MNRAS*, 345, 1057
- Miller, N. A., Mushotzky, R. F., & Neff, S. G. 2005, *ApJ*, 623, L109
- Pakull, M. W., & Grisé, F. 2008, in *A Population Exploration: the Nature & Evolution of X-ray Binaries in Diverse Environments*, *AIP Conf. Proc.* 1010, AIP, New York, p. 303
- Pakull, M. W., & Mirioni, L. 2002, online proceedings of the symposium 'New Visions of the X-ray Universe in the XMM-Newton and Chandra Era', 26–30 November 2001, ESTEC, The Netherlands (astro-ph/0202488)
- Pakull, M. W., & Mirioni, L. 2003, *Bubble Nebulae around Ultraluminous X-Ray Sources*, *Revista Mexicana de Astronomia y Astrofisica Conference Series*, Eds. J. Arthur & W. J. Henney, 15, 197.
- Pakull, M. W., Grisé, F., & Motch, C. 2006, in *Populations of High Energy Sources in Galaxies*, proc. of the IAU Symposium 230, eds E. J. A. Meurs and G. Fabbiano, Cambridge University Press, Cambridge, p. 293
- Pakull, M. W., Soria, R., & Motch, C. 2010, *Nature*, 466, 209
- Pannuti, T. G., Duric, N., Lacey, C. K., Ferguson, A. M. N., Magnor, M. A., & Mendelowitz, C. 2002, *ApJ*, 565, 966
- Park, S., Burrows, D. N., & Garmire, G. P. 2003, *ApJ*, 586, 210
- Pohl M., 1993, *A&A*, 270, 91
- Punsly, B. 2005, *ApJ*, 623, L9
- Prestwich, A. H., et al. 2007, *ApJ*, 669, L21
- Punsly, B. 2007, *MNRAS*, 374, L10
- Ramsey, C. J., Williams, R. M., Gruendl, R. A., Chen, C.-H. R., Chu, Y.-H., & Wang, Q. D. 2006, *ApJ*, 641, 241
- Rawlings, S., & Saunders, R. 1991, *Nature*, 349, 138
- Raymond, J. C., & Smith, B. W. 1977, *ApJS*, 35, 419
- Read, A. M., & Pietsch, W. 1999, *A&A*, 341, 8
- Remillard, R. A., & McClintock, J. E. 2006, *ARA&A*, 44, 49
- Roberts, T. P., Goad, M. R., Ward, M. J., & Warwick, R. S. 2003, *MNRAS*, 342, 709
- Russell, D. M., Fender, R. P., Gallo, E., & Kaiser, C. R. 2007, *MNRAS*, 376, 1341
- Sault, R. J., & Wieringa, M. H. 1994, *A&AS*, 108, 585
- Sault, R. J., Teuben, P. J., & Wright, M. C. H. 1995, *Astronomical Data Analysis Software and Systems IV*, 77, 433
- Scheuer, P. A. G. 1974, *MNRAS*, 166, 513
- Soria, R., Fender, R. P., Hannikainen, D. C., Read, A. M., & Stevens, I. R. 2006, *MNRAS*, 368, 1527
- Vancura, O., Blair, W. P., Long, K. S., & Raymond, J. C. 1992, *ApJ*, 394, 158
- Weaver, R., McCray, R., & Castor, J. 1977, *ApJ*, 218, 377
- Willott, C. J., Rawlings, S., Blundell, K. M., & Lacy, M. 1999, *MNRAS*, 309, 1017
- Wilson, A. S., Smith, D. A., & Young, A. J. 2006, *ApJ*, 644, L9

APPENDIX A: SYNCHROTRON EMISSION IN THE MINIMUM-ENERGY CONDITION

To estimate the minimum energy associated with the synchrotron-emitting cocoon, we assume an energy range ($\gamma_{\min}, \gamma_{\max}$) for the relativistic electrons (Pohl 1993; Bicknell 2005), rather than a frequency range. Typical empirical values of $\gamma_{\min} \sim 1-10$ (Blundell & Rawlings 2000) and $\gamma_{\max} \sim 10^4-10^5$. For a steep spectrum, the minimum energy depends only very weakly on the high-energy cut-off. We introduce the following quantities: ϵ_e is the energy density in relativistic electrons; $\epsilon_p \equiv (1+k)\epsilon_e$ is the energy density in relativistic particles (electrons and protons), where k is a free parameter; ϵ_B is the energy density in the magnetic field; $\epsilon_{\text{tot}} = \epsilon_p + \epsilon_B$ includes the energy in relativistic particles and magnetic field; ϵ'_{tot} is the total energy density including relativistic and non relativistic particles and the field. We introduce another free parameter $\eta \equiv \epsilon_{\text{tot}}/\epsilon'_{\text{tot}}$ to express the relative fraction of total energy stored in relativistic particles (protons and electrons) plus field. The main reason why we distinguish between ϵ_{tot} and ϵ'_{tot} is that there is solid observational evidence (Cavagnolo et al. 2010; Punsly 2007; Leahy & Gizani 2001; Willott et al. 1999) that most of the energy in the lobes and cavities of radio galaxies is in low-energy electrons and other non-relativistic particles (*i.e.* $\eta \ll 1$), and that the energy density of the magnetic field may be $\sim 10-100$ times less than the total energy density ϵ'_{tot} . Thus, using ϵ'_{tot} to derive a minimum-energy or equipartition criterion generally leads to very inaccurate estimates for the synchrotron emission of a lobe. Instead, here we apply those criteria only to ϵ_{tot} , that is we assume that magnetic energy density is of the same order of magnitude as the relativistic particle energy density but much less than the total particle energy density. And within the relativistic energy density component, we use the parameter k to express the relative contribution of nuclei and electrons.

Applying the minimum-energy condition leads, after some algebra (Bicknell 2005), to this expression for the

minimum-energy magnetic field:

$$\begin{aligned}
B_{\min}^2 &= \left(\frac{m_e}{e}\right)^2 \left[\frac{p+1}{2} (1+k) C^{-1}(p) \frac{c}{m_e}\right]^{4/(p+5)} \\
&\times \left[h(p, \gamma_{\min}, \gamma_{\max}) \frac{I_\nu \nu^{(p-1)/2}}{2r_c}\right]^{4/(p+5)} \\
&\approx \left(\frac{m_e}{e}\right)^2 \left(\frac{c}{m_e}\right)^{4/(p+5)} \left(\frac{3}{4\pi}\right)^{4/(p+5)} \\
&\times \left[\frac{p+1}{2} (1+k) C^{-1} h\right]^{4/(p+5)} d^{8/(p+5)} r_c^{-12/(p+5)} \\
&\times S_\nu^{4/(p+5)} \nu^{2(p-1)/(p+5)} \quad (\text{A1})
\end{aligned}$$

where the energy spectrum of the electrons is $N(E)dE \sim E^{-p}dE$, m_e and e are the electron mass and charge, c the speed of light, I_ν the specific surface brightness S_ν the specific flux at the observer's position, integrated over the whole cocoon, r_c is the cocoon radius, and d is the distance to the source. We have assumed a filling factor of 1, for simplicity. The functions

$$h(p, \gamma_{\min}, \gamma_{\max}) = \frac{1}{p-2} \left[\gamma_{\min}^{(2-p)} - \gamma_{\max}^{(2-p)} \right], \quad (\text{A2})$$

$$\begin{aligned}
C(p) &= \frac{3^{p/2}}{2^{(p+13)/2} \pi^{(p+2)/2}} \\
&\times \frac{\Gamma\left(\frac{p}{4} + \frac{19}{12}\right) \Gamma\left(\frac{p}{4} - \frac{1}{12}\right) \Gamma\left(\frac{p}{4} + \frac{1}{4}\right)}{\Gamma\left(\frac{p}{4} + \frac{7}{4}\right)}, \quad (\text{A3})
\end{aligned}$$

and $\Gamma(z)$ is the Gamma function. The corresponding total (minimum) energy density is:

$$\epsilon_{\text{tot},\min} = [(1+k)\epsilon_e + \epsilon_B]_{\min} = \left(\frac{4}{p+1} + 1\right) \left(\frac{B_{\min}^2}{2\mu_0}\right) \quad (\text{A4})$$

We now need to relate the energy density $\epsilon_{\text{tot},\min}$ to the input jet power and size of the bubble. An approximate expression we could use is that the total energy (relativistic, non relativistic and field) is simply $\mathcal{P}t$. However, this is not entirely correct, because part of the injected energy is spent to inflate the bubble. From the self-similar solution of Weaver et al. (1977), we obtain a more accurate expression for the energy still available:

$$\epsilon'_{\text{tot}} \equiv \frac{3}{4\pi} \frac{5}{11} \mathcal{P} t r_c^{-3}, \quad (\text{A5})$$

and according to our definition of η ,

$$\epsilon_{\text{tot}} \equiv \frac{3}{4\pi} \frac{5}{11} \eta \mathcal{P} t r_c^{-3}. \quad (\text{A6})$$

In the minimum-energy approximation, from Eq. A4:

$$\left(\frac{B_{\min}^2}{2\mu_0}\right) = \frac{3}{4\pi} \frac{5}{11} \eta \left(\frac{p+1}{p+5}\right) \mathcal{P} t r_c^{-3}, \quad (\text{A7})$$

and this value can now be substituted into Eq. A1. Finally, the cocoon radius r_c is obtained from the Weaver et al. (1977)'s set of self-similar solutions (assuming a thin outer shell):

$$r_c \simeq \left(\frac{125}{154\pi}\right)^{1/5} \times \left(\frac{\mathcal{P}t^3}{\rho_0}\right)^{1/5} \simeq 0.76 \times \left(\frac{\mathcal{P}t^3}{\rho_0}\right)^{1/5}, \quad (\text{A8})$$

and this expression is also substituted into Eq. A1. (Note that here it is the total jet energy $\mathcal{P}t$ that determines the size of the bubble).

Rearranging Eq. A1 with such substitutions, we obtain:

$$\begin{aligned}
S_\nu &\approx 1.84 \left(0.40 \eta \frac{p+1}{p+5}\right)^{(p+5)/4} \left(\frac{2\mu_0 e^2}{m_e^2}\right)^{(p+5)/4} \frac{m_e}{c} \\
&\times \left[\frac{p+1}{2} (1+k) C^{-1} h(p, \gamma_{\min}, \gamma_{\max})\right]^{-1} \\
&\times \mathcal{P}^{(p+11)/10} t^{(4-p)/5} \rho^{3(p+1)/20} \nu^{(1-p)/2} d^{-2}, \quad (\text{A9})
\end{aligned}$$

where the numerical values of h and C come from Eqs. (A2,3). For a spectral index $\alpha \approx -0.5$ ($p \approx 2$), $\gamma_{\min} \lesssim 10$ and $\gamma_{\max} \sim 10^5$, we have, in physical units:

$$S_\nu \approx 640 (1+k)^{-1} \eta^{7/4} \mathcal{P}_{39}^{1.3} t_5^{0.4} n_1^{0.45} d_1^{-2} \nu_5^{-0.5} \text{ mJy}, \quad (\text{A10})$$

where \mathcal{P}_{39} is the jet power in units of $10^{39} \text{ erg s}^{-1}$, t_5 is the source age in units of 10^5 yr , n_1 is the interstellar number density in cm^{-3} , d is the source distance in Mpc, ν_5 the observed frequency in units of 5 GHz; the numerical coefficient is not very sensitive to the choice of γ_{\min} . We can obtain an analogous estimate for a spectral index $\alpha \approx -0.7$ (corresponding to $p \approx 2.4$), which is more often the case in radio lobes. In that case,

$$S_\nu \approx 82 (1+k)^{-1} \eta^{1.85} \mathcal{P}_{39}^{1.34} t_5^{0.32} n_1^{0.51} d_1^{-2} \nu_5^{-0.7} \text{ mJy}, \quad (\text{A11})$$

where we have fixed this time $\gamma_{\min} = 1$.

We can now compare these specific fluxes with the observations: S26 has a 5.5-GHz flux $\approx 2 \text{ mJy}$, for a jet power \sim a few $10^{40} \text{ erg s}^{-1}$, at a distance of 3.9 Mpc. This tells us that $(1+k)^{-1} \times \eta^{1.85} \sim 10^{-3}$, that is the energy stored in synchrotron-emitting relativistic electrons (a fraction $\eta/(1+k)$ of the total) is much less than the energy stored in relativistic protons and in non-relativistic particles. We cannot determine the individual values of η and k from this set of radio observations alone: only their combination. If we use cosmic rays as an analogy (since they may be accelerated in jet and supernova shocks), we would expect $k \sim 100$. For plausible values $k \sim 10\text{--}100$, $\eta/(1+k) \sim$ few 10^{-3} .